

Free Wake Analysis of Helicopter Rotor Flow Fields Using a Coupled Vorticity Embedding / Fractional Step Method

A Thesis
Presented for the
Master of Science
Degree
The University of Tennessee, Knoxville

Jamie Ryan Kucab
August 2000

DISTRIBUTION STATEMENT A
Approved for Public Release
Distribution Unlimited

REPORT DOCUMENTATION PAGE

Form Approved
OMB NO. 0704-0188

Public Reporting burden for this collection of information is estimated to average 1 hour per response, including the time for reviewing instructions, searching existing data sources, gathering and maintaining the data needed, and completing and reviewing the collection of information. Send comment regarding this burden estimates or any other aspect of this collection of information, including suggestions for reducing this burden, to Washington Headquarters Services, Directorate for Information Operations and Reports, 1215 Jefferson Davis Highway, Suite 1204, Arlington, VA 22202-4302, and to the Office of Management and Budget, Paperwork Reduction Project (0704-0188), Washington, DC 20503.

1. AGENCY USE ONLY (Leave Blank)		2. REPORT DATE 11/27/00		3. REPORT TYPE AND DATES COVERED Final Technical Report May 1, 1995 - July 31, 2000	
4. TITLE AND SUBTITLE Free Wake Analysis of Helicopter Rotor Flow Fields Using a Coupled Vorticity Embedding/Fractional Step Method				5. FUNDING NUMBERS DAAH04-95-1-0258	
6. AUTHOR(S) Jamie Ryan Kucab, Graduate Research Assistant Dr. John Steinhoff, Principal Investigator					
7. PERFORMING ORGANIZATION NAME(S) AND ADDRESS(ES) The University of Tennessee Space Institute 411 B. H. Goethert Parkway Tullahoma, TN 37388-9700				8. PERFORMING ORGANIZATION REPORT NUMBER	
9. SPONSORING / MONITORING AGENCY NAME(S) AND ADDRESS(ES) U. S. Army Research Office P.O. Box 12211 Research Triangle Park, NC 27709-2211				10. SPONSORING / MONITORING AGENCY REPORT NUMBER ARO 34260.3-EG-AAS	
11. SUPPLEMENTARY NOTES The views, opinions and/or findings contained in this report are those of the author(s) and should not be construed as an official Department of the Army position, policy or decision, unless so designated by other documentation.					
12 a. DISTRIBUTION / AVAILABILITY STATEMENT Approved for public release; distribution unlimited.				12 b. DISTRIBUTION CODE	
13. ABSTRACT (Maximum 200 words) A hybrid CFD (Computational Fluid Dynamics) method combining a potential-based Vorticity Embedding method with an Euler solver is presented and validated for isolated rotor flows. First, a formulation of Vorticity Embedding is developed and validated for Cartesian grids. This formulation is utilized together with simple lifting lines to represent an isolated rotor in hover. The results for an isolated rotor are then compared with experiment. The method is then hybridized by coupling the Vorticity Embedding grid containing the rotor to a region containing a ground plane where a standard finite difference Euler solver is utilized. Initial results from this hybrid scheme are presented including a demonstration of the code's potential to calculate the ground vortex roll-up generated by a rotor in ground effect in the presence of a cross-wind.					
14. SUBJECT TERMS <div style="font-size: 2em; text-align: center;">20010117 057</div>				15. NUMBER OF PAGES 61	
				16. PRICE CODE	
17. SECURITY CLASSIFICATION OR REPORT UNCLASSIFIED		18. SECURITY CLASSIFICATION ON THIS PAGE UNCLASSIFIED		19. SECURITY CLASSIFICATION OF ABSTRACT UNCLASSIFIED	
				20. LIMITATION OF ABSTRACT UL	

Abstract

A hybrid CFD (Computational Fluid Dynamics) method combining a potential-based Vorticity Embedding method with an Euler solver is presented and validated for isolated rotor flows. First, a formulation of Vorticity Embedding is developed and validated for Cartesian grids. This formulation is utilized together with simple lifting lines to represent an isolated rotor in hover. The results for an isolated rotor are then compared with experiment. The method is then hybridized by coupling the Vorticity Embedding grid containing the rotor to a region containing a ground plane where a standard finite difference Euler solver is utilized. Initial results from this hybrid scheme are presented including a demonstration of the code's potential to calculate the ground vortex roll-up generated by a rotor in ground effect in the presence of a cross-wind.

Contents

1	Introduction	1
1.1	Rotor Analysis in Ground Effect	1
1.2	Review of Existing Methods	3
1.2.1	Vortex Methods	3
1.2.2	Euler and Navier-Stokes Fixed Grid Methods	4
1.2.3	Point-Lattice Methods	5
1.2.3.1	Cloud-in-Cell	5
1.2.3.2	Vorticity Embedding	6
1.3	Current Method	6
2	Numerical Method	7
2.1	Overview	7
2.2	Lifting Line Rotor Representation	8
2.3	Vorticity Embedding Region	11
2.3.1	Governing Equations	11
2.3.2	Vorticity Embedding	13
2.3.2.1	Complex-Lamellar Velocity Decomposition	13
2.3.2.2	The Clebsch Variables of Vorticity Embedding	14
2.3.2.3	Spreading	15
2.3.2.3.1	Computational vs. Physical Spreading	15
2.3.2.3.2	Weighted Averaging	15
2.3.2.4	Poisson Equation	16
2.3.2.5	Boundary Conditions	17
2.3.2.6	Staggered Computational Grid	18
2.3.2.7	Two Dimensional Implementation	19
2.4	Fractional Step Region	21
2.4.1	Governing Equations	21
2.4.2	Fractional Step Method	22
2.4.2.1	Staggered Computational Grid	22
2.4.2.2	Convection Step	24

2.4.2.3	Pressure Correction Step	25
2.4.3	Boundary Conditions	26
3	Previous Results	28
4	Current Results	30
4.1	Vorticity Embedding-Only Code	30
4.1.1	Lifting Line	32
4.1.1.1	Grid Dependence	32
4.1.1.2	Comparison with Caradonna & Tung data	33
4.1.1.3	Comparison with HELIX-I data	34
4.1.2	Comparison of Rotor Plane Computation with Experimental Results	35
4.2	Hybrid Code	38
4.2.1	Wake Segmentation	39
4.2.2	Optimization of q^v calculation	42
4.2.3	Boundary Overlap	42
4.2.4	Vortex Roll-up	43
5	Conclusions and Recommendations	46
	Bibliography	48
	Appendices	51
A	Nomenclature	52
A.1	Symbols	52
A.2	Superscripts	53
B	Image Point Convection	54
B.1	Equivalence with first upwind difference for appropriate Δt	54
B.2	Stability	55
C	"FISHPACK: A package of FORTRAN subprograms for the solution of separable elliptic partial differential equations"	56
D	q^v Computation Module	58
	Vita	61

List of Algorithms

1	HELIX-III Solution Procedure	8
2	Vorticity Embedding	12
3	Fractional-Step Method	23

Chapter 1

Introduction

1.1 Rotor Analysis in Ground Effect

The wake shed by a helicopter rotor is one of the most important factors in determining rotor performance. Unfortunately, the rotor wake is an extremely complicated aerodynamic feature. The saying that "a single helicopter blade faces more aerodynamic problems in one revolution than a fixed wing aircraft meets in its entire lifetime" [1] is particularly true when the blade in question is in proximity to the ground, that is, when the rotor is "in ground effect". In ground effect, the rotor wake becomes more complicated. A low advance ratio (ratio of free-stream or cross-wind to rotor tip speed) makes the rotor wake problem more complicated still while retaining the first-order impact of wake geometry on performance. Under these conditions, the free-stream and/or cross-stream interacts with the already complex rotor wake to produce a powerful ground vortex. This ground vortex (visualized in Figure 1.1 [6] using helium bubbles) wraps around the helicopter and causes an array of problems including loss of yaw control. In other cases, the ground vortex can interact negative-

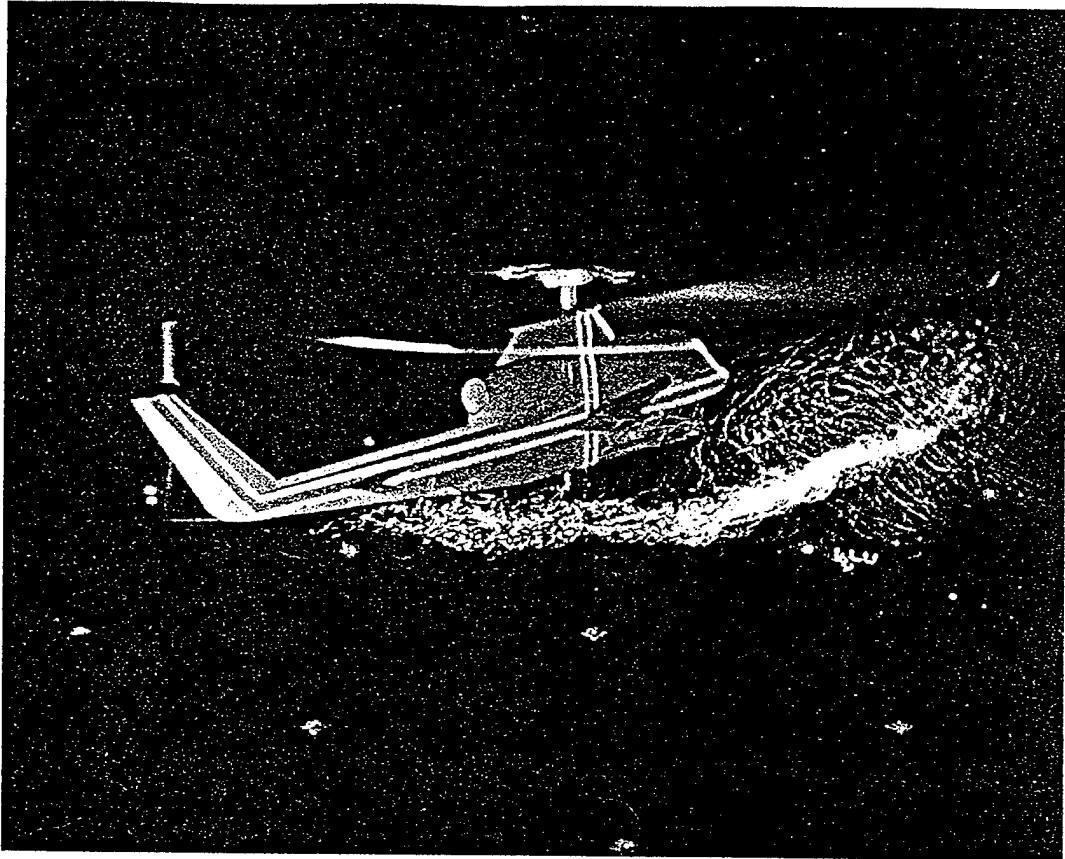


Figure 1.1: Ground Vortex Impinging on Empennage

ly with the main rotor or with other aircraft in formation. Also, the helicopter wake can interact with ground operations or ship deck operations.

In general, the computation of rotors in near-ground operation requires the ability to predict both the wake structures shed by the blades and the larger vortex structures along the ground. It is the purpose of this paper to investigate the effectiveness of the Vorticity Embedding method coupled with a conventional Euler solver to predict the wake and ground vortex structures mentioned above. An existing but previously incomplete and undocumented code (called HELIX-III) will be used for this purpose.

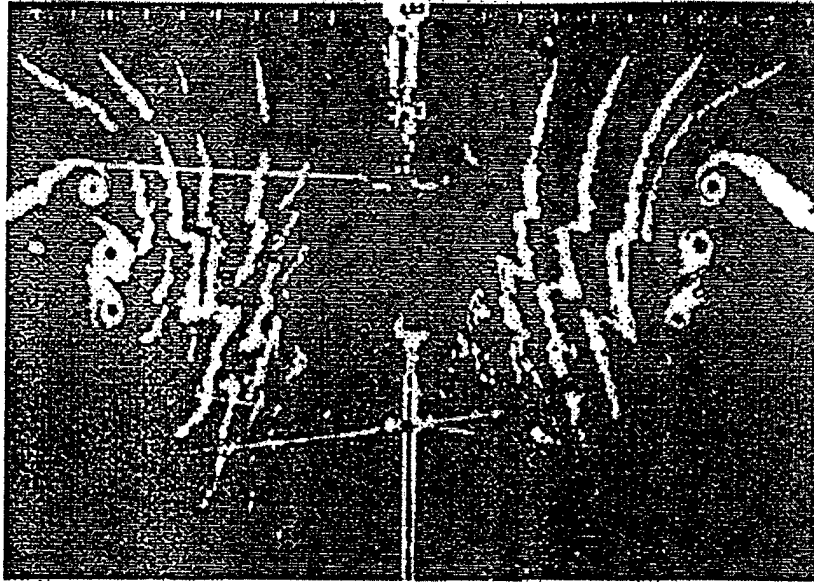


Figure 1.2: Smoke Visualization of Rotor Wake (taken from [11])

1.2 Review of Existing Methods

The flow field created by a rotor is characterized by thin regions of vorticity in an otherwise potential flow. The smoke visualization of a rotor wake in Figure 1.2 which is diagrammed in Figure 1.3 clearly shows the velocity discontinuity caused by the thin region of vorticity which comprises the wake. It also clearly shows the powerful tip vortices caused by the roll-up of the rotor wake. Many methods have been devised to treat the problems which are associated with calculating flows containing regions of compact vorticity.

1.2.1 Vortex Methods

Vortex methods treat the wake as a sheet of Lagrangian vortex filaments using the Biot-Savart law to calculate the velocity induced by the filaments. Determining ve-

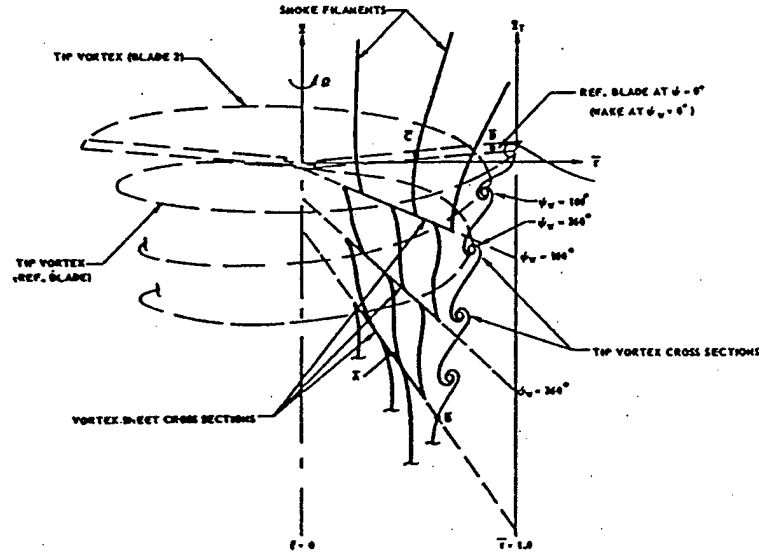


Figure 1.3: Diagram of Smoke Visualization (adapted from [11])

locity at a point requires calculation of the influence of all vortex filaments on that point. Vortex methods have been used in conjunction with other methods providing inflow values to potential, Euler or Navier-Stokes solvers.

1.2.2 Euler and Navier-Stokes Fixed Grid Methods

Conceptually, Euler and Navier-Stokes solvers greatly simplify the process of calculating a rotor flow. They can predict both the load on the rotor and the associated wake in a uniform manner free of artificial constructs such as wake markers. In actuality, the efforts necessary to achieve adequate grid resolution near the wake (adaptive grid refinement, overset and/or unstructured grids) tend to complicate this approach. The wake has been found experimentally to be as thin as 5% of the chord. Supposing it requires 12 points across the thinnest part of the wake to adequately

1.2. REVIEW OF EXISTING METHODS

resolve the wake and it is desired to maintain this resolution down to one radius below the plane of a rotor with blade aspect ratio of 15, then this grid will require $2 * \pi * \left(15 * \frac{12}{0.05}\right)^3 = 2.9 * 10^{11}$ points. And even then the "solution" obtained on this grid will be only a model of the Navier-Stokes equations for the vortex core region which can be turbulent with even smaller length scales. At present, a rotor wake computation of 10 million ($1.0 * 10^7$) points is considered very large and requires tens or even hundreds of hours on expensive, specialized supercomputers. Therefore, the usefulness of Euler and Navier-Stokes solvers is limited to regions in the flow field either very near the blade where adequate grid resolution can be achieved or in regions far enough removed from the rotor that the rotor wake no longer has a first-order impact on the blade loadings. The former justification was used in employing an overset Navier-Stokes solver in the HELIX-I code to determine the flow near the rotor blade [12]. The latter justification is used in employing an Euler solver to determine flow near the ground in the HELIX-III code.

1.2.3 Point-Lattice Methods

1.2.3.1 Cloud-in-Cell

The cloud-in-cell or vortex-in-cell method utilizes a Lagrangian wake convected by its own induced velocity which is calculated on an Eulerian grid. By calculating the wake-induced velocity on an Eulerian grid and interpolating the velocities back to the wake in order to convect it, an artificial viscosity is inherently introduced by truncation error which has the benefit of eliminating the singularity present in Biot-Savart methods. This is a two dimensional method. [13]

1.2.3.2 Vorticity Embedding

Vorticity Embedding (VE) is a Lagrangian technique for modeling the wake created by a lifting body. Like other Lagrangian methods it avoids the numerical diffusion associated with standard Eulerian methods. VE satisfies the Euler equations (integrated though the wake sheet) rather than satisfying the Biot-Savart law, so its usefulness is not limited to incompressible flow like traditional Lagrangian methods. Further, calculation of velocity at a point does not require calculating the influence of every filament/point/blob on that point. Therefore, it is computationally inexpensive compared to more traditional vortex methods. [19]

1.3 Current Method

This particular method utilizes a lifting line together with a VE solver to model the rotor wake. This solver is then coupled to a fractional step (FS) solver to model the interaction of the rotor wake with a ground plane.

HELIX-III was originally conceived by Prof. Steinhoff and implemented - without the lifting line - by Dr. M. Moulton and Dr. S. Babu. It was passed on to the author after Dr. Babu's departure from UTSI. The code required a couple of corrections and implementation of the lifting line. The required corrections and the addition of the lifting line are the goals of this work.

Chapter 2

Numerical Method

2.1 Overview

The computational region is spanned by two Cartesian Eulerian grids which have one or more coincident planes (perpendicular to the z -axis) as shown in Figure 2.1. In the "upper" or "rotor" region, we utilize a lifting line to represent the rotor and Vorticity Embedding to model the wake while in the "lower" or "ground" region, a conventional fractional step Euler solver is employed. Hereafter, these regions will be referred to as the Vorticity Embedding or VE region and the fractional step or FS region, respectively. The overall solution procedure for the HELIX-III is outlined in Algorithm 1.

The previously mentioned HELIX-I code has been used extensively for the computation of hover flows where a blade-fixed (rotating) cylindrical H-grid proved to be most convenient. In a blade-fixed grid (and neglecting the fuselage), hover flow is steady and blade-to-blade periodic making it possible to compute the entirety of the desired flow-field based on a single blade. In forward flight or in the presence of

2.2. LIFTING LINE ROTOR REPRESENTATION

Algorithm 1 HELIX-III Solution Procedure

1. Advance the rotor blade (lifting line) by $\Delta\theta$ (usually one or two degrees).
 2. Perform the lifting line calculation to get the circulation (or enforce a fixed circulation) to impose on the new wake markers which are added at the new rotor position.
 3. Calculate the velocities in the VE region using the velocity of the FS region from the previous time step to calculate the flux BC for the interface boundary.
 4. Calculate the velocities in the FS region using the velocity from the VE region for the velocity BC at the interface.
 5. Repeat the above steps until sufficiently converged
-

a cross-wind, such simplifications are no longer possible. Therefore, HELIX-III has been devised based on a uniform Cartesian grid. This erases the distinction between hover and forward flight. Further, it allows HELIX-III to be coupled to another solver in order to better resolve flow near the ground.

2.2 Lifting Line Rotor Representation

Since the grid is non-rotating, the rotor must move through the grid. Typically, this is accomplished with some type of oversetting wherein an inner blade-fixed grid communicates with the Cartesian grid by interpolation. At present, this type of method is not employed because only the general flow field, especially near the ground, is required. Therefore, a lifting line rotor representation is utilized. In this approach, the rotor blade is represented as a line vortex and requires no special gridding. The strength of the sheet is the local rotor circulation. This is obtained by computing a local rotor inflow angle (requiring an interpolation from the Cartesian velocity field

2.2. LIFTING LINE ROTOR REPRESENTATION

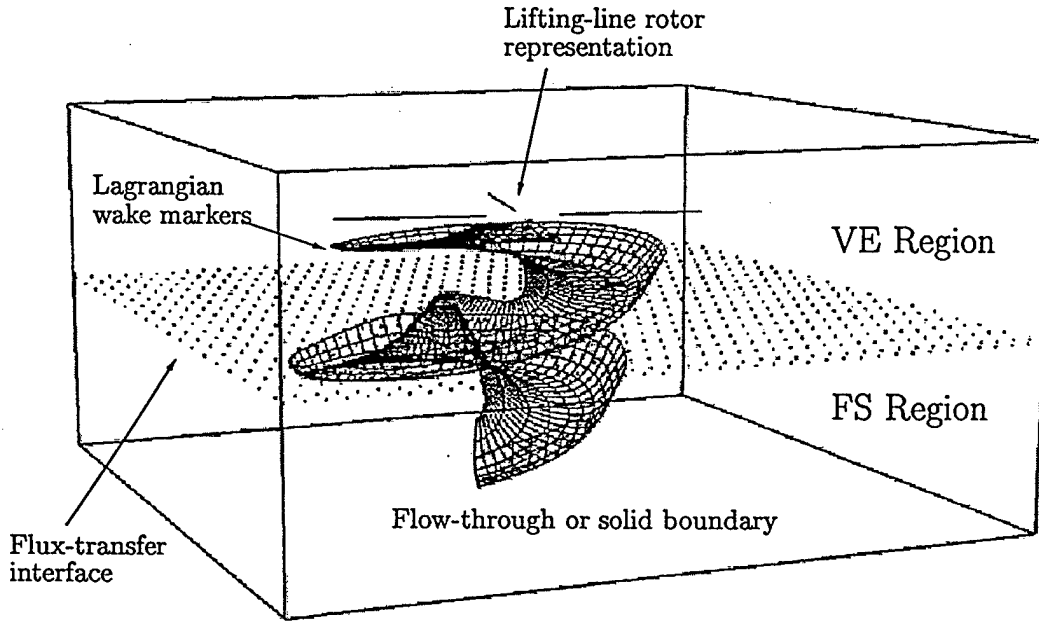


Figure 2.1: HELIX-III Overview

to the lifting line) and assuming a local, ideal two dimensional flow to obtain the circulation.

The local angle of attack is the sum of the collective pitch and the inflow angle which is calculated as follows:

$$\alpha_i = -\arctan\left(\frac{w_\infty}{\frac{r}{R}\Omega}\right) \quad (2.1)$$

where w_∞ is the downward component of the local free-stream velocity which may be adjusted to include a downward contribution from the bound vortex associated with the leading edge of the wake sheet. That is,

$$w_\infty = w_i + \frac{\Gamma}{2\pi d}, \quad (2.2)$$

2.2. LIFTING LINE ROTOR REPRESENTATION

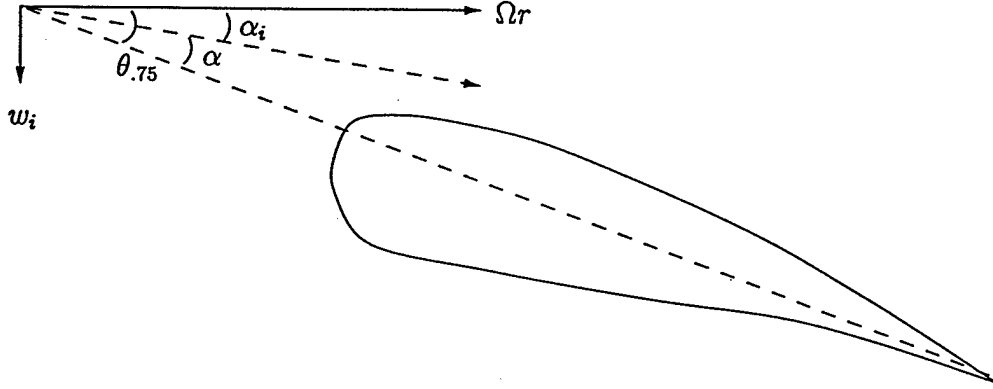


Figure 2.2: Lifting Line

where d is the distance to the leading edge of the wake sheet. This requires a tri-linear interpolation of the downward component of velocity, w_i , at a point one chord ahead of the leading edge of the wake sheet. The sectional lift coefficient is then computed according to thin airfoil theory,

$$c_l = 2\pi\alpha \quad (2.3)$$

where

$$\alpha = \theta_{.75} + \alpha_i. \quad (2.4)$$

The circulation associated with a marker originating at the leading edge of the wake sheet is

$$\Gamma = \frac{C_l}{2} \left(\frac{r}{R} \Omega \right). \quad (2.5)$$

This lifting line approximation provides reasonable results to within one chord of the blade tip where the two dimensional assumption is no longer valid. Therefore, within one chord of the tip, the circulation is continued quadratically to zero.

2.3 Vorticity Embedding Region

In the Vorticity Embedding region, the flow is determined by the rotor wake. It is necessary to adequately resolve the rotor wake for at least one blade passage, as there is a pronounced effect on the blade loading. Therefore, Vorticity Embedding is used in this region. Vorticity Embedding is a computationally efficient way of embedding a thin layer of vorticity (the wake) around Lagrangian markers in an otherwise potential flow. This method is the basis of the HELIX-I code which has been used successfully for the prediction of hover performance of isolated rotors [15],[16]. The Lagrangian nature of the wake convection eliminates the need for extremely high grid densities (to prevent diffusion) and allows thin regions of high vorticity to be convected over distances large enough to accurately model several revolutions of the rotor wake.

The overall solution procedure for the VE region is found in Algorithm 2.

2.3.1 Governing Equations

Typical rotor tip speeds place the embedding region in the compressible flow regime. However, for simplicity and to permit the use of available direct solvers, the present implementation is incompressible. Therefore, the incompressible version of the continuity equation,

$$\nabla \cdot \mathbf{q} = 0, \quad (2.7)$$

is satisfied in the VE region. The circulation introduced into the flow by the lifting lines is preserved according to Kelvin's theorem:

$$\frac{D\Gamma}{Dt} = 0. \quad (2.8)$$

2.3. VORTICITY EMBEDDING REGION

Algorithm 2 Vorticity Embedding

1. Calculate the Clebsch functions on the grid nodes within the spreading distance of the Lagrangian-marker-wake-sheet.
 - (a) Calculate the sheet strength (circulation), Γ .
 - (b) Calculate the shape function, λ .
 2. Calculate the rotational component of velocity, \mathbf{q}^v , according to equation 2.12
 3. Calculate the irrotational component of the velocity field, $\nabla\phi$.
 - (a) Calculate ϕ such that
$$\nabla^2\phi = -\nabla \cdot \mathbf{q}^v. \quad (2.6)$$
 - (b) The irrotational component is $\nabla\phi$.
Therefore, velocity (2.11) satisfies the continuity equation (2.7).
 - (c) Set $\mathbf{q}^v = \mathbf{q}^v + \nabla\phi$
 - (d) Extrapolate new boundary conditions
 - (e) Repeat (a)-(d) until \mathbf{q}^v is sufficiently divergence-free.
Then $\mathbf{q} = \mathbf{q}^v$.
 4. Stop if sufficiently converged; otherwise, convect the wake markers using the two-step Runge-Kutta method and start over.
-

2.3. VORTICITY EMBEDDING REGION

The circulation around a material loop changes only at the lifting line, as that loop is convected through the VE region.

2.3.2 Vorticity Embedding

2.3.2.1 Complex-Lamellar Velocity Decomposition

It is typical of velocity decompositions to represent the velocity as the sum of a vortical component and the gradient of a scalar, that is,

$$\mathbf{q} = \mathbf{q}^v + \nabla\phi. \quad (2.9)$$

Because the curl of the gradient of a scalar is zero, the vorticity is entirely contained within the the vortical component, so

$$\boldsymbol{\omega} = \nabla \times \mathbf{q} = \nabla \times \mathbf{q}^v. \quad (2.10)$$

One such decomposition is the complex-lamellar^{1,2} decomposition. Here, the velocity decomposition takes the following form:

$$\mathbf{q} = \Gamma \nabla \lambda + \nabla \phi \quad (2.11)$$

¹ \mathbf{q}^v is a complex-lamellar flow field if it can be divided by an integrating function, Γ , to produce a potential or "lamellar" flow [14]:

$$\frac{\mathbf{q}^v}{\Gamma} = \nabla \lambda$$

²Equivalently, a complex-lamellar vector field is any vector field which is perpendicular to its own curl [14], that is

$$\mathbf{q}^v \cdot (\nabla \times \mathbf{q}^v) = 0$$

2.3. VORTICITY EMBEDDING REGION

where the three variables $(\Gamma, \nabla, \lambda)$ are sometimes called Clebsch variables. The complex-lamellar decomposition is very interesting in that the Clebsch variables can be chosen such that $q^v = 0$ when $\omega = 0$ [14].

2.3.2.2 The Clebsch Variables of Vorticity Embedding

Vorticity Embedding is based on a particular complex-lamellar velocity decomposition. The Clebsch variables are chosen such that the vortical component, q^v , is only non-zero in a thin region surrounding the Lagrangian wake markers. Said vortical component is defined as

$$q^v \equiv -\Gamma \nabla \lambda \quad (2.12)$$

where Γ is the circulation and λ is an as yet arbitrary shape function. For computational simplicity, q^v is chosen such that it is perpendicular to the wake sheet [19]. Therefore the circulation is

$$\Gamma = \int q^v \cdot d\hat{n} \quad (2.13)$$

where the integration is performed normal to the sheet. In terms of a traditional potential flow solver, the integral of q^v must equal the local potential jump, Γ , across the sheet of shed vorticity. For convenience, λ is chosen to be a half-sine wave whose zero-crossing is at the sheet:

$$\lambda \equiv \frac{1}{2} \sin \left(\frac{\pi S_n}{2 \bar{a}} \right) \quad (2.14)$$

where S_n is the signed normal distance from the sheet and \bar{a} is the spreading parameter which determines the number of cells over which the vortex sheet is spread or "smeared".

2.3. VORTICITY EMBEDDING REGION

2.3.2.3 Spreading

2.3.2.3.1 Computational vs. Physical Spreading In its original formulation, VE utilized physical spreading. The Clebsch variables were calculated within a given physical distance of the wake sheet. Using physical spreading, a search is performed from each Eulerian grid point to find the Lagrangian wake markers that fall within the physical spreading distance. The Clebsch variables on that Eulerian grid point are then calculated based on a weighted average of the contributions from all of the markers that fall within the physical spreading distance of the grid point. The use of computational spreading was previously proposed [17] and implemented [12] wherein the Clebsch variables were calculated in computational space rather than physical space. Now, \bar{a} represents a computational distance, or number of cells, from the sheet over which the Clebsch variables are calculated. Additionally, instead of iterating over Eulerian grid points, the procedure was changed to iterate over the Lagrangian wake markers (a 2-D structure rather than a 3-D structure).

2.3.2.3.2 Weighted Averaging Because each Eulerian grid point can be influenced by multiple wake markers, Γ and S_n (for the calculation of λ per 2.14) must be treated as a weighted average from all wake markers that are within the selected region of influence. Therefore,

$$\Gamma_{i,j,k} = \frac{1}{A} \left[\sum_{\ell} \left(\sum_{i,j,k} \Gamma^{\ell} \sigma_{i,j,k}^{\ell} \right) \right] \quad (2.15)$$

and

$$(S_n)_{i,j,k} = \frac{1}{A} \left[\sum_{\ell} \left(\sum_{i,j,k} S_n^{\ell} \sigma_{i,j,k}^{\ell} \right) \right] \quad (2.16)$$

2.3. VORTICITY EMBEDDING REGION

where i, j, k are the Eulerian grid indices, ℓ is the wake marker index, $\sigma_{i,j,k}^\ell$ is the ratio of the difference between the spreading distance and the distance to the grid point to the spreading distance squared defined by

$$\sigma_{i,j,k}^\ell = \max \left(0, 1 - \frac{|\mathbf{x}_{i,j,k} - \chi^\ell|^2}{a^2} \right) \quad (2.17)$$

where $\mathbf{x}_{i,j,k}$ is the position of the grid point and χ^ℓ is the position of the wake marker and A is the sum of these ratios,

$$A = \sum_{\ell} \left(\sum_{i,j,k} \sigma_{i,j,k}^\ell \right). \quad (2.18)$$

The current numerical procedure for normalization (multiplying $\Gamma_{i,j,k}$ and $(S_n)_{i,j,k}$ by $\frac{1}{A}$) requires us to iterate over all the grid points. This defeats the intentions of the change in the Clebsch procedure from iterating over grid points to iterating over wake markers. The Clebsch calculation again necessitates iterating over a 3-D structure rather than just over a 2-D structure (the wake sheet) as might be expected. Further, it has unfortunate consequences when we increase the number of wake sheets to eliminate unintended averaging.

2.3.2.4 Poisson Equation

Given the rotational component of velocity, \mathbf{q}^v , we can now calculate the irrotational component of the velocity, $\nabla\phi$. We require that $\nabla\phi$ exactly cancel out the divergence

2.3. VORTICITY EMBEDDING REGION

created by the rotational component of velocity. Therefore,

$$\nabla \cdot \nabla \phi = \nabla^2 \phi = -\nabla \cdot \mathbf{q}^v \quad (2.19)$$

providing us with a Poisson equation to solve for the potential ϕ . The regular grid allows us to use a fast direct Poisson solver from FISHPACK [see Appendix C]. The only other things necessary to calculate the irrotational velocity component are the appropriate boundary conditions.

2.3.2.5 Boundary Conditions

In the simplest case: an isolated rotor in hover without coupling to a ground region (the FS region); Dirichlet boundary conditions are employed. The flow is assumed to be normal to the boundary surface. This is accomplished by using a non-homogeneous lower boundary condition.

$$\phi = \int q_r^v dr \quad (2.20)$$

where q_r^v is the radial component of \mathbf{q}^v and the integration is performed radially, in from the outer edge of the wake region.

The aforementioned non-homogeneous lower boundary condition is no longer appropriate given the presence of a ground (FS) region to which it is coupled. Instead, the flux across the boundary is calculated, based on the velocity from the coincident plane of the FS region (from the previous time step) and the vortical velocity from the wake sheet according to the following equation:

$$\frac{\partial \phi}{\partial n} = (\mathbf{q}_{FS}^{n-1} - \mathbf{q}_{VE}^v) \cdot \hat{\mathbf{n}}, \quad (2.21)$$

2.3. VORTICITY EMBEDDING REGION

which follows from the definition of the total velocity in the VE region as the sum of an irrotational and rotational velocity. In this case, the irrotational component is calculated from the total velocity (extrapolated from the interior of the FS region) and the rotational component from the VE region. For all of the other boundaries, a homogeneous Dirichlet conditions are initially imposed followed by repeated solution of the Poisson equation with Dirichlet boundary conditions extrapolated from the previous solution until convergence is reached.

2.3.2.6 Staggered Computational Grid

A staggered 128x128x32 regular Cartesian grid is used. The scalar variables (ϕ , Γ , λ , etc.) are stored at the node points and the vector quantities (q and q^v) are located at the cell centers. This is convenient as gradients and divergences can be approximated using a box scheme. In 2-D for example,

$$(\nabla \cdot q^v)_{i,j} \simeq \frac{q_{i+\frac{1}{2},j}^v - q_{i-\frac{1}{2},j}^v}{\Delta x} + \frac{q_{i,j+\frac{1}{2}}^v - q_{i,j-\frac{1}{2}}^v}{\Delta y}$$

and

$$(\nabla \phi)_{i,j} \simeq \hat{i} \frac{\phi_{i+\frac{1}{2},j} - \phi_{i-\frac{1}{2},j}}{\Delta x} + \hat{j} \frac{\phi_{i,j+\frac{1}{2}} - \phi_{i,j-\frac{1}{2}}}{\Delta y}$$

where for example $q_{i+\frac{1}{2},j}^v \equiv \frac{1}{2} (q_{i+\frac{1}{2},j+\frac{1}{2}}^v + q_{i+\frac{1}{2},j-\frac{1}{2}}^v)$ and the other values with integral indices are similarly defined.

In previous implementations of VE, the calculation of the Clebsch variables required a computationally expensive search to locate the Lagrangian wake points [12]. In the present implementation, this search is reduced to a simple mapping by the use of a regular Cartesian grid. Also, the regular Cartesian grid simplifies the process of

2.3. VORTICITY EMBEDDING REGION

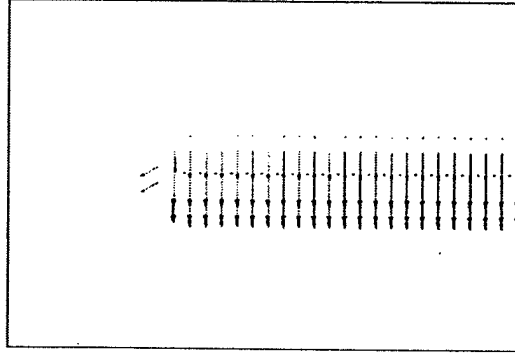


Figure 2.3: q^v

calculating the Clebsch variables as physical spreading and computational spreading become synonymous.

2.3.2.7 Two Dimensional Implementation

As part of this investigation, a two dimensional version of Vorticity Embedding was briefly implemented. Some results from this implementation are presented here to help illustrate the VE solution process.

Figure 2.3 shows a two dimensional q^v field generated by a "lifting point" and a trailing straight line wake which is analogous to the branch cut in a traditional potential flow calculation. A line integral of the component of q^v perpendicular to the line of markers taken about the edge of the line of markers will recover the circulation Γ imposed at the leading edge of wake markers and hence on all of the markers shown. Figure 2.4 is the divergence-free velocity field associated with the q^v distribution in Figure 2.3 and Figure 2.5 is that velocity plus a constant free-stream velocity.

2.3. VORTICITY EMBEDDING REGION

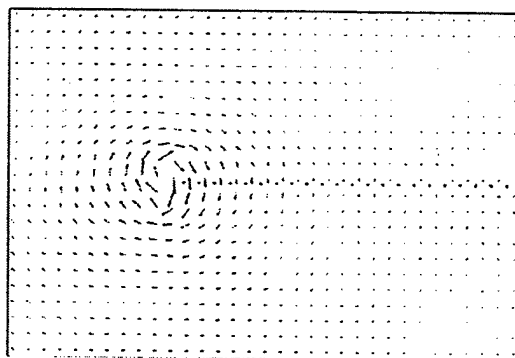


Figure 2.4: $\mathbf{q}^v + \nabla\phi$

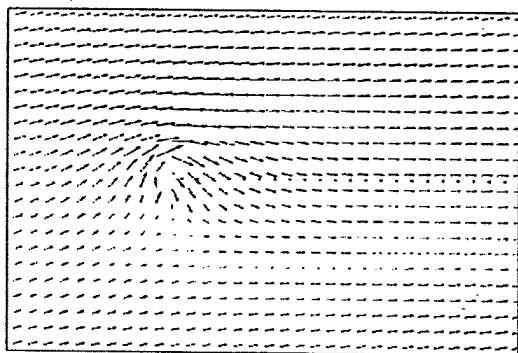


Figure 2.5: \mathbf{q}

2.4 Fractional Step Region

The HELIX-III code will be used for calculations in which a ground plane is present. In the presence of a ground plane, the wake structure becomes complex. Physically, we see that without a free stream velocity, the rotor wake system expands outward along the ground in rings of increasing diameter. In the presence of a free-stream velocity, the ground vortex forms a horseshoe shape with the ends of the horseshoe pointing downstream. The wake near the ground on the free-stream side stops expanding at some point as the velocity induced by the wake becomes equal to the free stream velocity. At this "stagnation point" [6], the wake rolls up into a concentrated ground vortex. Lagrangian methods (VE included) become cumbersome when a ground plane enters the computation. Not only are wall boundary conditions problematic, but a computationally expensive decision process for combining the wake vortex elements is necessary. Fortunately, the individual wake identities are not important to the rotor loads at this distance. It was the efficiency of the VE method for accurately approximating the effects of these individual wake elements that originally prompted the use of VE in the region near the rotor. Therefore, a conventional solver is employed in the region near the ground.

2.4.1 Governing Equations

In the FS region, we assume that the flow is incompressible and inviscid. The equations governing the physics of three-dimensional incompressible inviscid flow are the incompressible Euler equations: the momentum equation,

$$\partial_t \mathbf{q} = -(\mathbf{q} \cdot \nabla) \mathbf{q} - \nabla P, \quad (2.22)$$

2.4. FRACTIONAL STEP REGION

where P is pressure divided by the constant density and the continuity equation,

$$\nabla \cdot \mathbf{q} = 0. \quad (2.23)$$

2.4.2 Fractional Step Method

Equations 2.22 and 2.23 (together with appropriate boundary conditions) form a well-posed set of differential equations [9]; however, the absence of an evolution equation for the pressure makes constructing a straight forward numerical method difficult.

The *fractional step method*³ (also commonly referred to as a *projection method*⁴) provides a way to evolve a solution to the incompressible Euler equations in time. In this case, the incompressible three-dimensional Euler equations are broken up into convection and mass balance equations which are solved sequentially. The overall procedure is illustrated in Algorithm 3.

2.4.2.1 Staggered Computational Grid

The fractional-step computation is also made on a 128x128x32 staggered grid. The pressure values are stored at the grid nodes and all of the velocity components are stored at the cell-centers. A portion of a two dimensional version of this grid is shown in Figure 2.6 . A similar grid was used in [7] with a similar fractional step method with

³Temam uses this title. Temam proposed the method in 1969. Yanenko applies the title to the more general class of methods which includes ADI, LOD, etc. [21]

⁴This title was popularized by Chorin's justification for the method as a *projection method* in the sense that the velocity is projected from the nonsolenoidal intermediate velocity field into a solenoidal (divergence-free) subspace. [4], [3] This category of projection method is not related to another category of projection methods which includes Galerkin's method and the method of collocation except for their common application to certain partial differential equations. Galerkin's method and the method of collocation are called projection methods, because they suppose a solution exists in an infinite-dimensional function space and *project* the solution onto a finite-dimensional subspace according to basis functions. [8, pg 179]

Algorithm 3 Fractional-Step Method

1. The convection step

(a) Enforce the velocity BC (taking the upper boundary velocity from the rotor grid)

(b) Calculate the first intermediate velocity, q^*

$$q^* = q^n - \Delta t (q^n \cdot \nabla) q^n \quad (2.24)$$

2. The pressure correction step yields q^{**}

(a) Initial BC for P :

$$P = 0 \quad (2.25)$$

and subsequent BC for P :

$$P = P_{extrap} \quad (2.26)$$

except at the ground boundary where the tangency condition is enforced. This leads to

$$\frac{\partial P}{\partial n} = \frac{1}{\Delta t} (q^* \cdot \hat{n}). \quad (2.27)$$

(b) Calculate P such that

$$\nabla^2 P = \frac{1}{\Delta t} \nabla \cdot q^*. \quad (2.28)$$

(c) Then calculate the second intermediate velocity

$$q^{**} = q^* - \Delta t \nabla P \quad (2.29)$$

(d) Repeat (a) through (c) until P converges.

3. Apply smoothing to q^{**} , to obtain the final velocity:

$$q^{n+1} = q^{**} + c \nabla^2 q^{**}$$

where c is chosen arbitrarily to keep the method stable (currently, $c = .01$). The necessity of this smoothing step was found by Dr. Babu and was accepted unquestioningly by the author.

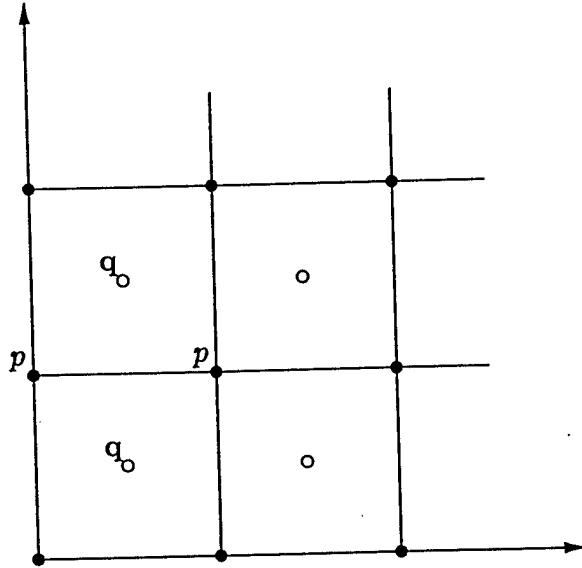


Figure 2.6: The fractional-step method staggered grid in two dimensions

the exception that the pressures were located at the cell-centers and the velocities at the nodes.

2.4.2.2 Convection Step

The time-discrete momentum equation is

$$\mathbf{q}^{n+1} = \mathbf{q}^n - \Delta t(\mathbf{q}^n \cdot \nabla) \mathbf{q}^n - \Delta t \nabla P^{n+1} \quad (2.30)$$

or

$$\mathbf{q}^{n+1} = \mathbf{q}^* - \Delta t \nabla P^{n+1} \quad (2.31)$$

where

$$\mathbf{q}^* = \mathbf{q}^n - \Delta t(\mathbf{q}^n \cdot \nabla) \mathbf{q}^n. \quad (2.32)$$

2.4. FRACTIONAL STEP REGION

The calculation of q^* constitutes the convection step. This calculation is performed using a first order "image point" method which is attributed to [5]. This method can be shown to be equivalent to the first order explicit upwind scheme for appropriate choice of Δt (see Appendix B for explanation and equivalence with first order explicit upwind scheme).

2.4.2.3 Pressure Correction Step

Now, to find P^{n+1} , we take the divergence of 2.30:

$$\nabla \cdot q^{n+1} = \nabla \cdot q^* - \Delta t \nabla^2 P^{n+1} \quad (2.33)$$

and according to the continuity equation (2.23), $\nabla \cdot q^{n+1} = 0$. Therefore, we are left with the *pressure Poisson equation*:

$$\nabla^2 P^{n+1} = \frac{1}{\Delta t} \nabla \cdot q^*. \quad (2.34)$$

Equation 2.34 is solved using a routine from FISHPACK. The gradient of the resulting pressure is then added to the first intermediate velocity, q^* , in the pressure correction step. The resulting velocity, q^{**} , then automatically satisfies the continuity equation (2.23) as can be seen here:

$$\nabla \cdot q^{**} = \nabla \cdot q^* - \Delta t (\nabla \cdot \nabla P) = 0. \quad (2.35)$$

Finally, smoothing is added to the second intermediate velocity to obtain the velocity at time $n + 1$.

2.4.3 Boundary Conditions

The appropriate pressure boundary conditions for the fractional step method is a topic that causes much confusion (at least for the author). This is particularly true for outflow boundary conditions (see [18] for examples of the variety of BCs employed). For the outflow boundaries (sides, downstream), we approximate “fully developed flow”, that is, $\frac{\partial u^*}{\partial n} \rightarrow 0$ by extrapolating Dirichlet boundary conditions from the interior. The inflow boundary conditions (upstream, upper) are simpler. The upstream boundary is the specified free-stream velocity (or is the same as the sides if there is no free-stream). The upper boundary velocities are taken from the coincident plane of the VE region. The lower boundary condition is no flow through (tangency) if a ground is present and outflow (as described above) otherwise.

The pressure boundary conditions are also extrapolated from the interior. However, as no evolution equation exists for the pressure, we are not able to obtain an interior solution without boundary conditions. Therefore, it is necessary to assume incorrect homogeneous Dirichlet boundary conditions in order to obtain an interior solution. This interior solution is then extrapolated to the boundaries to provide non-homogeneous Dirichlet boundary conditions. These extrapolated BC are then presumably less incorrect. This extrapolation to the boundaries is repeated until sufficiently correct boundary conditions are obtained. The only exception to this procedure is in the case where a solution with a ground plane present is desired. In this case, a Neumann boundary condition is found by taking the dot product of Equation 2.31 and the outward pointing normal yielding

$$\frac{\partial \phi}{\partial n} = -\frac{1}{\Delta t} (q_n^{n+1} - q_n^*) \quad (2.36)$$

2.4. FRACTIONAL STEP REGION

which must be homogenous in order to satisfy the no-flow-through condition.

Chapter 3

Previous Results

One of Dr. Babu's original (unpublished) results is shown in Figure 3.1 . This result is for a Sikorsky UH-60A rotor. This is an untapered blade with an aspect ratio, AR , of 15.5. For both cases, the tip Mach number, M_t , is 0.63. The blade circulation is fixed from a previous solution using the HELIX-I code, that is, the lifting line procedure described in section 2.2 was not used. The code that generated the data for these images represents the starting point for this investigation.

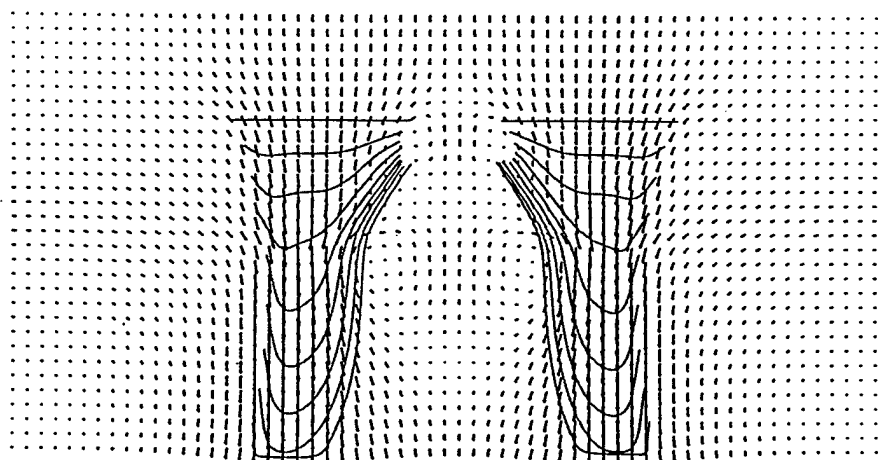


Figure 3.1: UH-60A Rotor in Hover with no Ground (Original Hybrid Code)

Chapter 4

Current Results

Two problems can be seen in Figure 3.1. First, there is a lack of velocity near the inboard portion of the wake which leads to unacceptable stretching of the wake sheet. And second, a plot of the divergence reveals mass conservation errors at the interface. These mass errors can also be seen as unaccounted for variations in the velocity field at the interface. As it was also desired to extend the code by the addition of a lifting line calculation to obtain the circulation to impose on the leading edge of the sheet, it was necessary to split HELIX-III up into two different codes: a VE-only code for for extending HELIX-III by adding the lifting line and the original hybrid version to test changes to the code to alleviate the two aforementioned problems.

4.1 Vorticity Embedding-Only Code

Vorticity contours and tip vortex trajectories calculated from the results of a hover case run with this VE-only code are shown in Figure 4.1. After the results of the lifting line are examined, comparisons will be made between the wake geometry shown

4.1. VORTICITY EMBEDDING-ONLY CODE

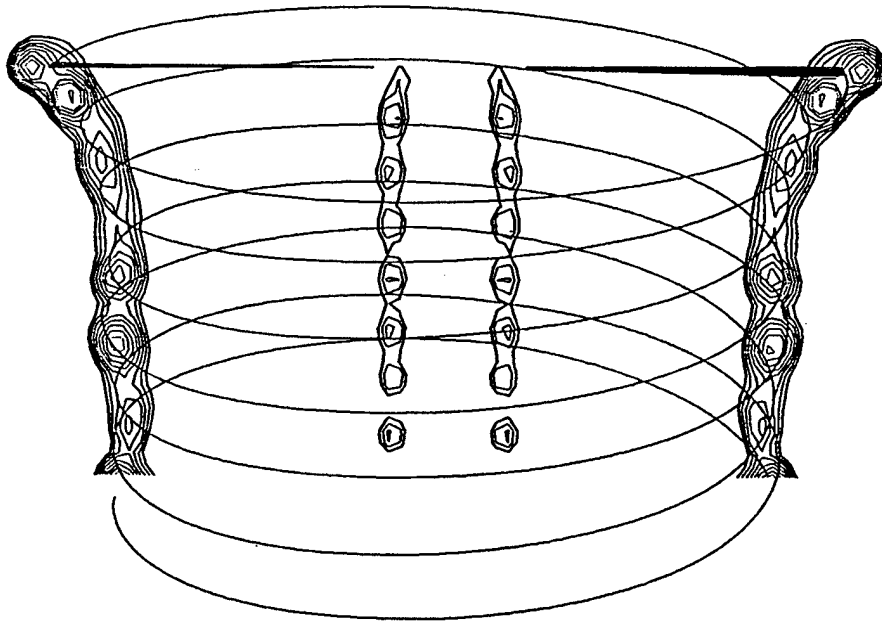


Figure 4.1: Vortex Core Trajectories and Vorticity Contours

4.1. VORTICITY EMBEDDING-ONLY CODE

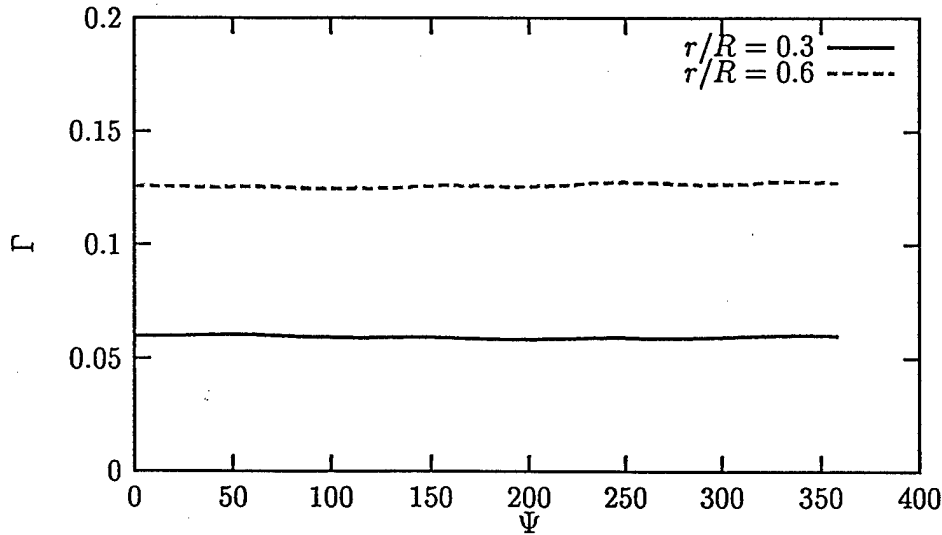


Figure 4.2: Variation of circulation due to Cartesian grid

here and wake geometries obtained from experimental data.

4.1.1 Lifting Line

4.1.1.1 Grid Dependence

The interpolation of w introduces a small grid dependence in the calculated inflow, w_i . Therefore, it was necessary to determine the consistency of this approximation before assessing the accuracy. To this end, an inflow was calculated at each of two points and recorded for one revolution. Figure 4.2 illustrates the magnitude of the variation at these two points on the lifting line. The inflow calculation varied by less than 3% at each of the points and, therefore, was judged to be sufficiently consistent.

4.1. VORTICITY EMBEDDING-ONLY CODE

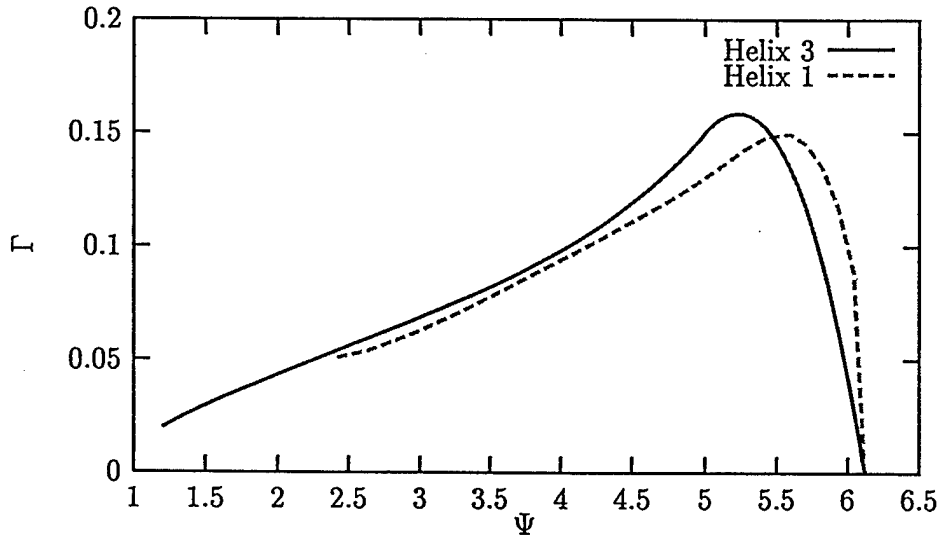


Figure 4.3: Caradonna & Tung Rotor Circulation, HELIX-III vs. Data (Calculated Inflow)

4.1.1.2 Comparison with Caradonna & Tung data

The circulation, Γ , obtained by the lifting line calculation detailed in section 2.2 was compared to experimental data from [2]. The results were acceptable for this particular rotor (AR=6, untwisted, untapered NACA 0012). The lifting line assumption becomes invalid near both the inboard and outboard tips of each blade and there requires an extrapolation based on the inboard values and the physical requirement that the circulation goes to zero at both the inboard and outboard tips. Figure 4.3 compares the circulations calculated by the lifting line in HELIX-III with those obtained by experiment in [2]. The circulation results obtained compare well even for this lower aspect ratio blade (6).

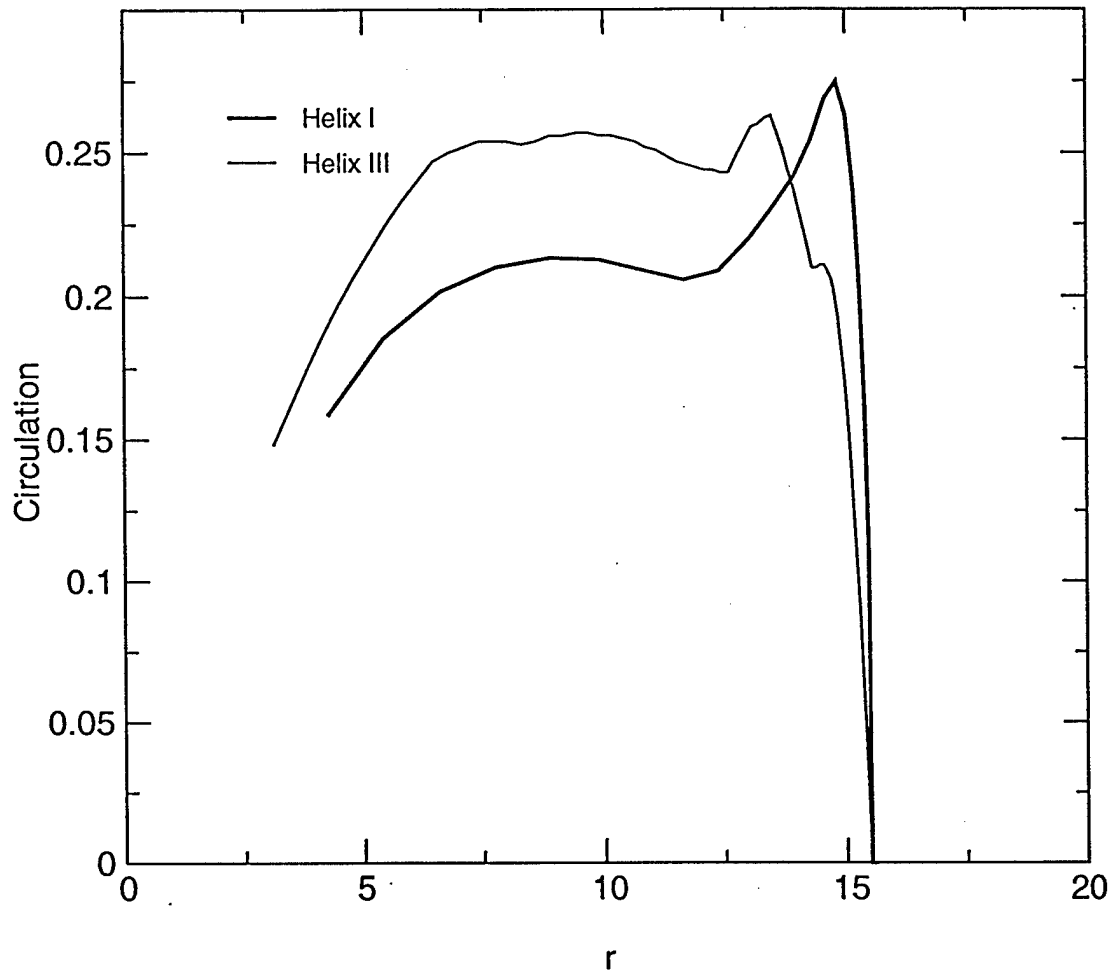


Figure 4.4: UH-60A Circulation, HELIX-I vs. HELIX-III (Fixed Inflow)

4.1.1.3 Comparison with HELIX-I data

Having validated the lifting line representation of the rotor with the experimental data from [2], a lifting line computation was then conducted for the UH-60A rotor. The calculated circulation was then compared to previously validated results from HELIX-I. The less than satisfactory results of this comparison are shown in Figure 4.4. This led to a thorough re-examination and re-implementation of the lifting line with the

4.1. VORTICITY EMBEDDING-ONLY CODE

same less than satisfactory results. This calculation was made without allowing the circulation actually imposed at the leading edge to vary, that is, the calculation was made based on an inflow that was created by a wake with the desired circulation. If the circulation that is imposed at the leading edge was changed according to the calculated circulation, the circulation distribution "evolves" to that shown in Figure 4.5. The location of the lifting line (one half chord forward of the leading edge of the wake sheet) was the only parameter in the calculation that was not taken strictly from theory, and this was taken from standard procedures of panel theory calculations. It was proposed that the standard procedures of panel methods might not work with Vorticity Embedding and that the appropriate location of the lifting line might be other than one half chord in front of the leading edge of the sheet. The location was iterated over from zero chords to one-and-one-half chords forward from the leading edge of the wake sheet and up to one-and-a-half chords above the plane of rotation. The best of these results was still unsatisfactory. Attempting to account for the contribution of bound vorticity to the effective angle of attack according to Equation 2.2 did not significantly improve the results. It was then proposed that the inflow be averaged azimuthally about the rotor disk at each radial station and this inflow value be used in the lifting line computation. The slightly more encouraging results from this further simplification are shown in Figure 4.6.

4.1.2 Comparison of Rotor Plane Computation with Experimental Results

The results from the HELIX-III code have been compared to a variety of data obtained from experiment. In Figure 4.7, the radial position of the tip vortex computed by

4.1. VORTICITY EMBEDDING-ONLY CODE

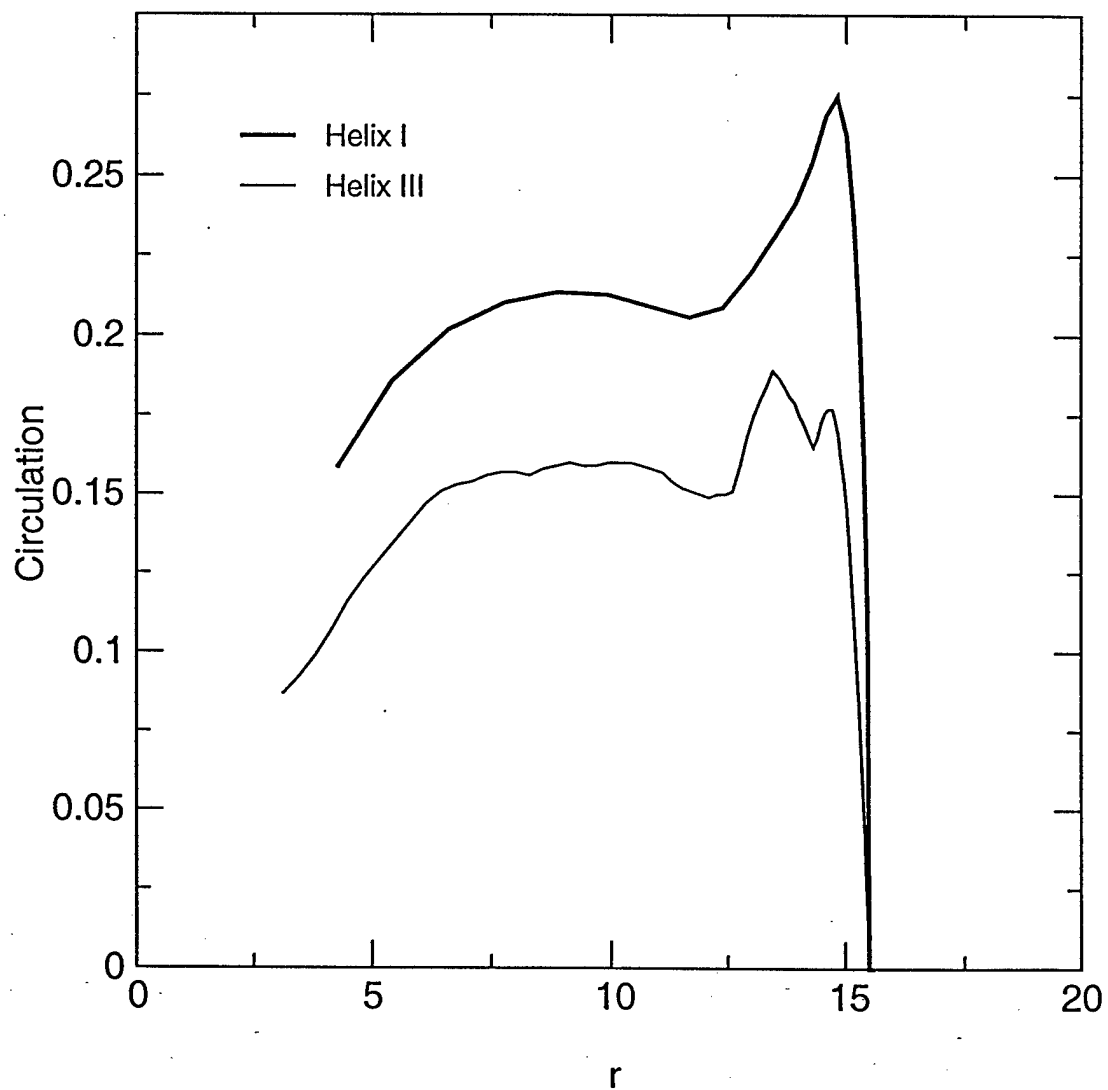


Figure 4.5: UH-60A Circulation, HELIX-I vs. HELIX-III (Calculated Inflow)

4.1. VORTICITY EMBEDDING-ONLY CODE

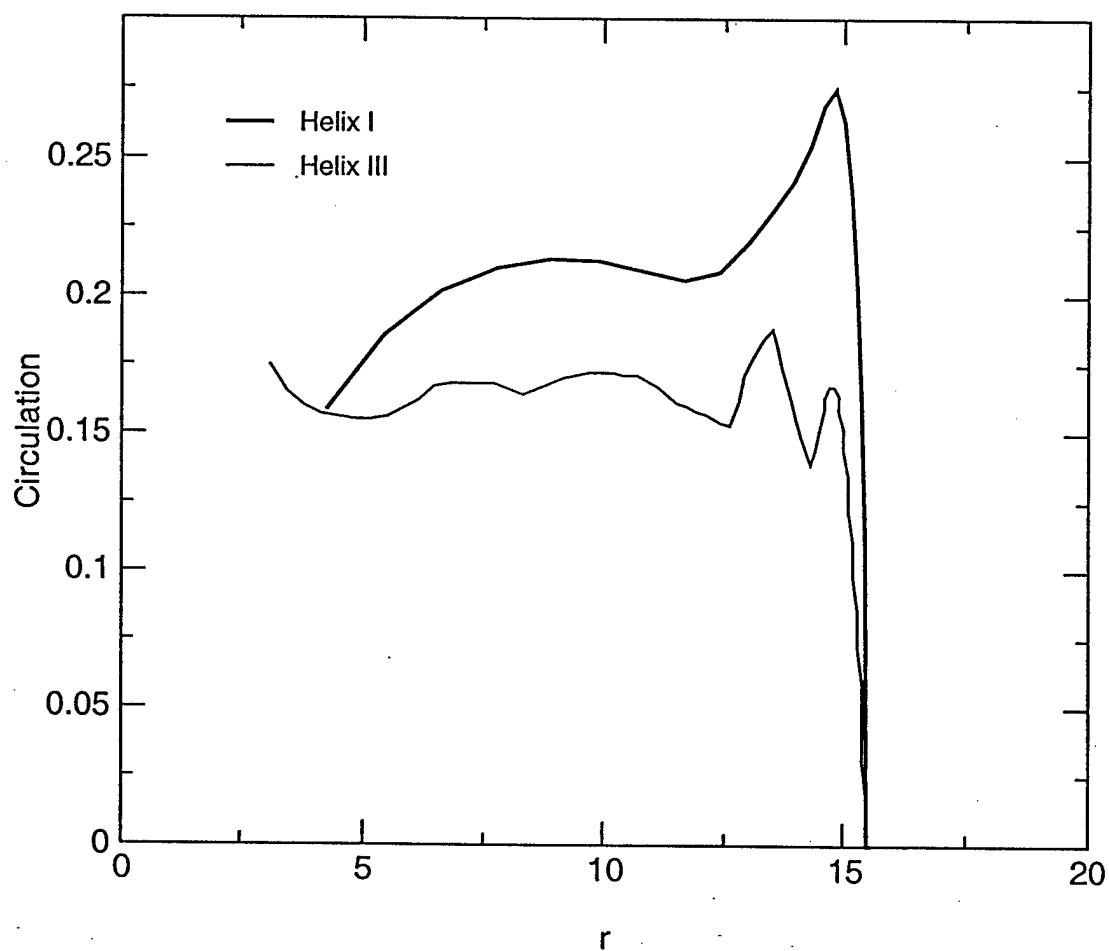


Figure 4.6: UH-60A Circulation, HELIX-I vs. HELIX-III (Azimuthally Averaged In-flow)

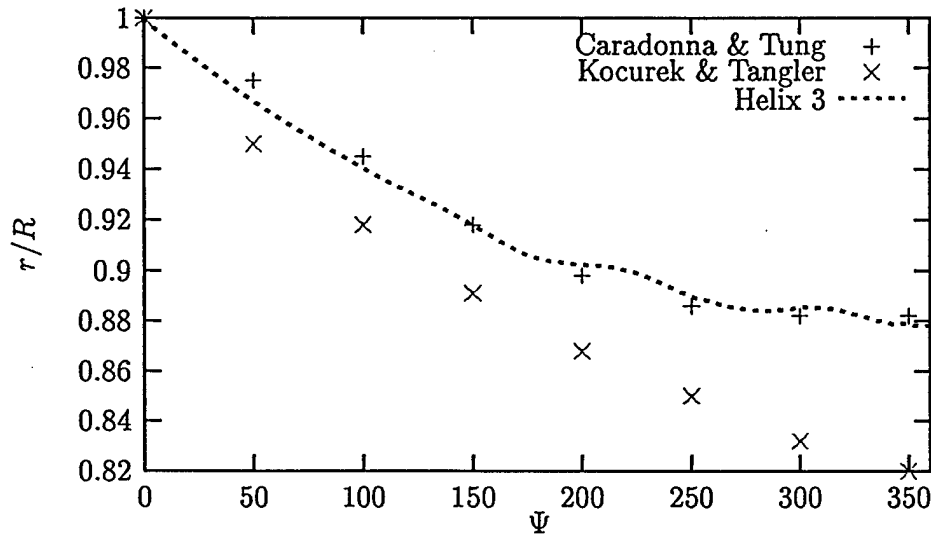


Figure 4.7: Wake Contraction

HELIX-III is compared with the radial position of the tip vortex measured in the experiments of [10] and [2]. A two-bladed rotor with an aspect ratio of 6 was used in both experiments. The low aspect ratio makes the lifting line assumption invalid for a large section of the blade, but the results still compare well with experiment. For perspective, the contraction predicted by simple momentum theory is also plotted. In Figure 4.8, the vertical position of the tip vortex is plotted for one revolution. The experimental data was taken from the same sources as above.

4.2 Hybrid Code

In the hybrid code, the interface to the FS region is included; however, the lifting line calculation is not attempted. Instead a fixed circulation, $\Gamma \equiv \Gamma(r)$, is taken from another solution. In this case, the circulation is taken from a UH-60A calculation performed with the HELIX-I code. Two modifications were performed on this code.

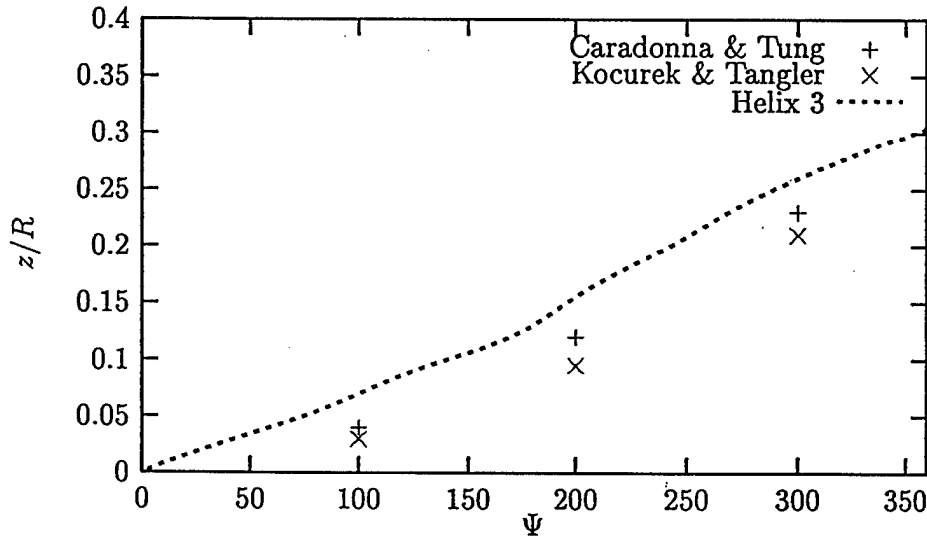
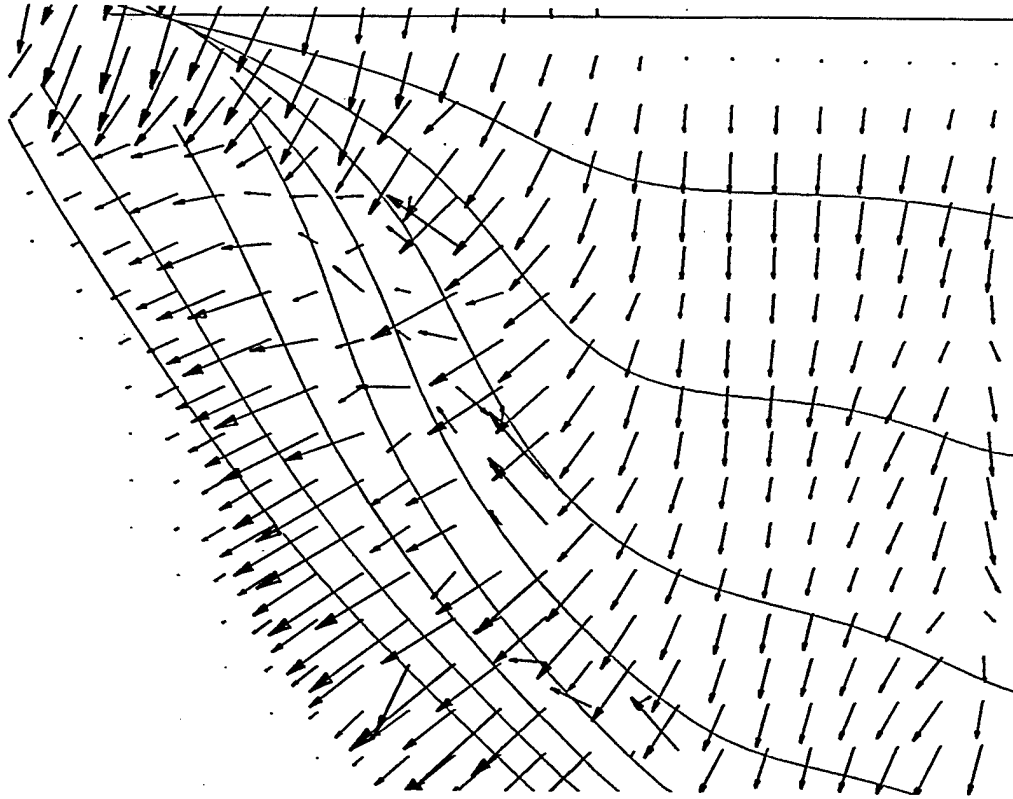


Figure 4.8: Wake Geometry

First, the wake was broken up into segments to prevent overwriting in the calculation of the Clebsch variables. Second, the number of coincident planes between the two solvers was increased in order to prevent mass errors.

4.2.1 Wake Segmentation

The computational spreading approach to calculating the Clebsch variables involves iterating over each sheet of wake markers (a 2D structure) rather than the grid nodes (a 3D structure). This results in a significant savings in time, but leads to complications when resolving the wake for multiple revolutions. Wake panels located further down the wake (azimuthally) wrap around and come close to newer wake panels from the same sheet. The aforementioned weighted averaging (see Section 2.3.2) is no longer appropriate when the wake panels are not neighboring panels but are still part of the same sheet. This leads to the overwriting of Γ and λ . The effect of the over-

Figure 4.9: Unsegmented q^v Field

writing can be seen as an inappropriate lack of velocity wherever the the sheets are closely layered over top one another. This necessitates breaking up the wakes of each of the blades into segments of less than 180° . A q^v field generated by an unsegmented Clebsch variable calculation is shown in Figure 4.9. A q^v field generated by the Clebsch/ q^v routines after segmentation is shown in Figure 4.10. Breaking each sheet up into segments and calculating the Clebsch variables for each segment rather than each sheet ensures that non-local panels of a single sheet will have an additive effect on the q^v field rather than inappropriately canceling each other out according to the

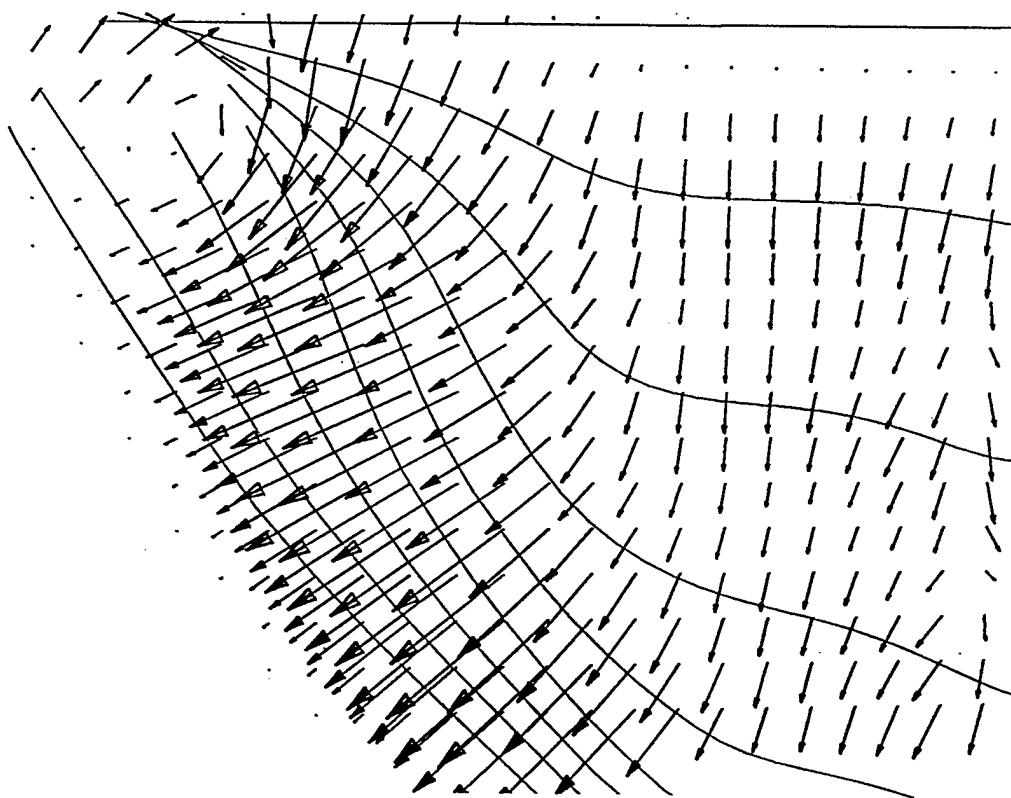


Figure 4.10: Segmented q^v Field

averaging logic.

An unexpected benefit to this wake segmentation is the ease with which this will allow for parallelization of the code. The individual contributions of the wake segments to the overall q'' field are independent of each other allowing for simple parallelization for the case where the number of processors is less than or equal to the number of wake segments.

4.2.2 Optimization of q'' calculation

The segmentation of each wake sheet leads to an increase in computational time, particularly in the calculation of q'' from the Clebsch variables. In order to keep computation times reasonable it was necessary to perform some optimization of the calculation of q'' . The sequence of if-then statements that determined whether grid points were above or below the sheet or at the edges was reduced to an algebraic mapping. The actual changes to the code are detailed in Appendix D. These changes reduced the overall computational time with segmentation by almost 40%. Without segmentation, the reduction in computational time was around 15%.

4.2.3 Boundary Overlap

For the upper boundary of the FS region, it is necessary to compensate for the small error introduced by the lower boundary condition in the VE region. An overlap region is created where at least four planes of the VE region and the FS region are coincident. The velocity boundary condition for the convection step of the FS region is then taken from a distance of five cells from the lower boundary of the VE region. The pressure boundary condition for the upper boundary of the FS region is unaffected by the

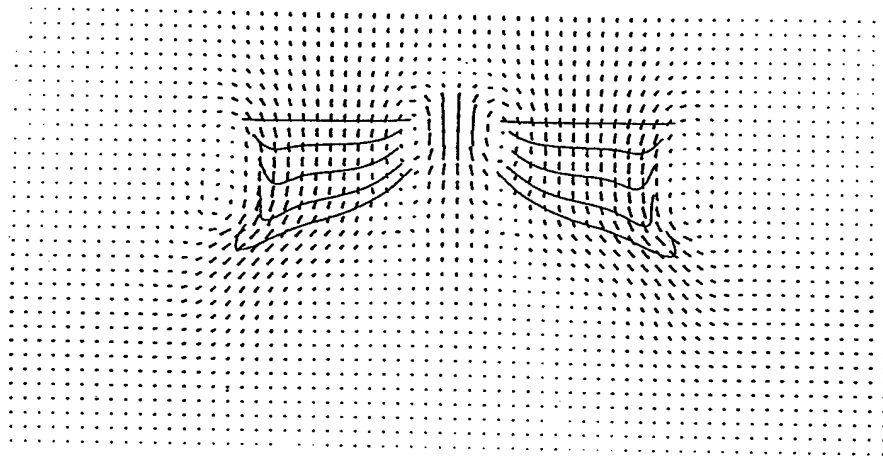


Figure 4.11: Rotor in Ground Effect. Calculation Made with Segmentation but without Increased Overlap.

interface and proceeds as previously described. This change reduced the maximum divergence by 21%. Qualitative changes to the velocity field are demonstrated in Figures 4.11 (without the increased overlap) and 4.12 (with the increased overlap).

4.2.4 Vortex Roll-up

The eventual goal for this code is to approximate the flow fields of rotors in ground effect in the presence of a cross-wind. To this end, a calculation was made for a UH-60A rotor in ground effect with a cross-wind. The results of a particle trace through

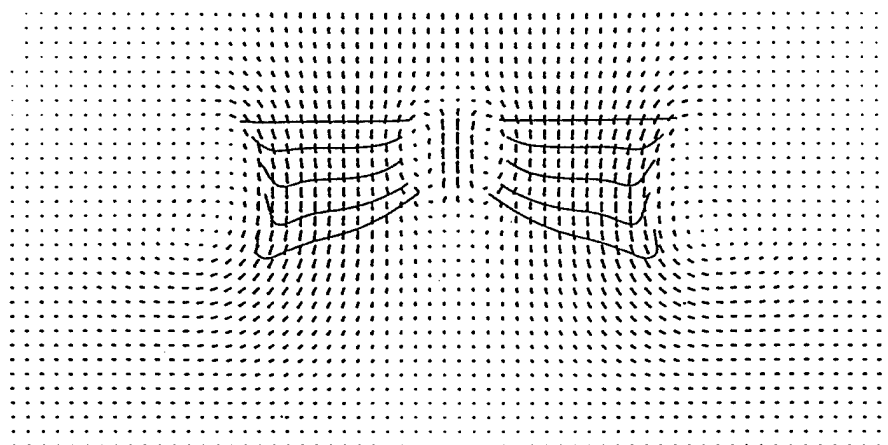


Figure 4.12: Rotor in Ground Effect. Calculation Made with Segmentation and Increased Overlap.

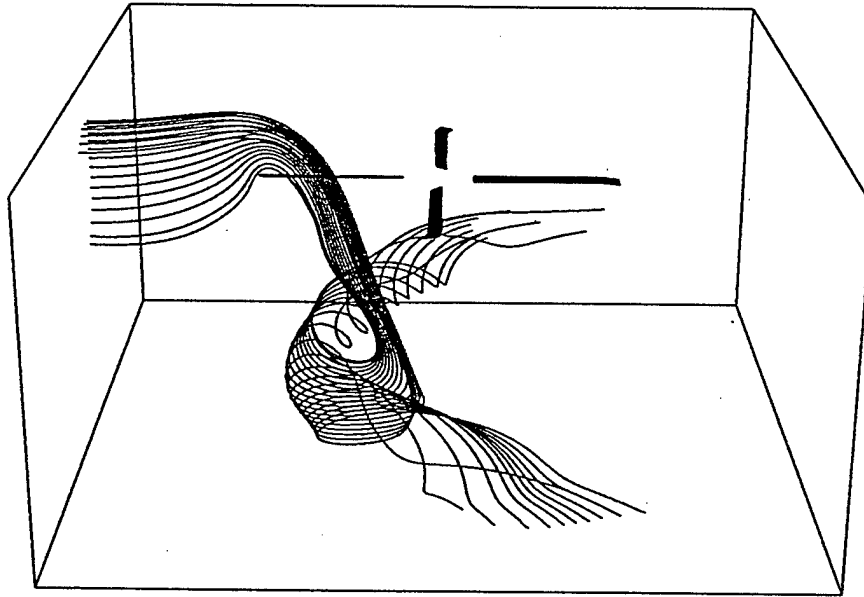


Figure 4.13: Isolated UH-60 Rotor in Forward Flight

this flow field is shown in Figure 4.13. This clearly shows the expected horseshoe-shaped ground vortex.

Chapter 5

Conclusions and Recommendations

Promising results have been obtained for the hybrid version of the HELIX-III code. The code was compared to both experiment and previous computational results. This demonstrated that the calculated wake geometry is acceptable. The calculated lift coefficients were acceptable in one case and less than acceptable in the other case. Qualitatively good results were found for the roll-up of the ground vortex. Finally, this paper will serve as documentation for a code that otherwise may never have been documented.

There are a few remaining problems. First and most important, it must be possible to calculate the correct circulation to impose on the wake markers. The current lifting line method is not sufficiently accurate. The cause of this is unknown. An overset grid about the blade may be a better solution. The overset grid could take advantage of the flow solver already implemented for the FS region or an established solver could be coupled to the embedding region as is the case with the HELIX-I code. To simplify things, the could be used only for the calculation of circulation, that is, the velocities calculated in this blade around the solver would only be used to calculate

CONCLUSIONS AND RECOMMENDATIONS

the circulation to be imposed at the leading edge of the sheet. Velocity boundary conditions would be interpolated from the Eulerian grid and appropriate circulations would be output.

The second remaining problem with the HELIX-III code is speed. This lack of speed is caused by two things. First, the extrapolation of boundary conditions for the Poisson equations in both the VE and FS regions. Currently, five iterations of the Poisson solver are needed to extrapolate values of ϕ and p at the boundaries. In most fractional step methods, homogeneous Neumann BC are utilized for the pressure calculation. To use Neumann BC we need the pressure defined at the cell-centers and the velocity defined at the nodes, because FISHPACK requires the forcing function (divergence of the previous intermediate velocity) to be supplied at the boundaries wherever Neumann conditions are imposed. Unfortunately, because of the coupling of this solver to the VE solver, this will require changes beyond the scope of this work.

Finally, the grid independence of the solutions obtained was never demonstrated. This was pointed out towards the end of the work and was left out due to time constraints. However, this is a basic step necessary for the validation of CFD results, and is, therefore, the next logical step for the complete validation of the previously obtained results.

BIBLIOGRAPHY

Bibliography

- [1] Baals, Donald D. and Corliss, William R. "Wind Tunnels of NASA". SP 440 NAS 1.21:440; 629.134'52 81-607811 AACR2, NASA, Washington, D.C., 1981.
<http://www.hq.nasa.gov/office/pao/History/SP-440/cover.htm>.
- [2] Caradonna, F. X. and Tung, C. "Experimental and Analytical Studies of a Model Helicopter Rotor in Hover". Technical report, NASA TM-81232, 1981.
- [3] Chorin, Alexandre Joel. *Computational Fluid Mechanics*. Academic Press, 1969.
- [4] Chorin, Alexandre Joel. On the convergence of discrete approximations to the navier-stokes equations. *Mathematics of Computation*, 23, 1969.
- [5] Courant, R., Isaacson, E. and Rees, M. On the solution of nonlinear hyperbolic differential equations by finite differences. *Communications on Pure and Applied Mathematics*, 5:243-255, 1952.
- [6] Empey, R. W. and Ormiston, R.A. "Tail-Rotor Thrust on a 5.5-Foot Helicopter Model in Ground Effect". Paper presented at the 30th Annual National Forum of the American Helicopter Society, Washington, D. C., May, 1974.
- [7] Fortin, M., Peyret, R. and Temam, R. Résolution numérique des équations de navier-stokes pour un fluide incompressible. *Journal de Mecanique*, 10(3), September 1971.
- [8] Golub, Gene H. and Ortega, James M. *Scientific Computing and Differential Equations*. Academic Press, Inc., 1992.
- [9] Johnson, Richard W., editor. *The Handbook of Fluid Dynamics*, chapter 31, pages 9-10. CRC Press, 1998.
- [10] Kocurek, J. D. and Tangler, J. L. "A Prescribed Wake Lifting Surface Hover Performance Analysis". Proceedings of the AHS 32nd Annual Forum and Technology Display, Washington, D.C., No. 1001:1-12, May 10-12, 1976.

-
- [11] Landgrebe, A. J. "An Analytical and Experimental Investigation of Helicopter Rotor Hover Performance and Wake Geometry Characteristics". USAAMRDL Technical Report 71-24, Eustis Directorate, U.S. Army Air Mobility Research and Development Laboratory, Ft. Eustis, VA, June 1971.
- [12] Moulton, M. A. "Zonal Procedure for Predicting the Hover Performance of a Helicopter Rotor". PhD thesis, University of California, Davis, 1998.
- [13] Murman, E. M. and Stremel, P. M. A vortex wake capturing method for potential flow calculations. AIAA Paper 82-0947, June 1982.
- [14] Panton, Ronald L. *Incompressible Flow*. John Wiley and Sons, 1984.
- [15] Ramachandran, K. *Free-Wake Analysis of Helicopter Rotor Blades in Hover Using a Finite-Volume Technique*. PhD thesis, University of Tennessee, Knoxville, TN, 1987.
- [16] Ramachandran, K., Owen, S. J., Caradonna, F. X. and Moffitt, R. C. "Hover Performance Prediction Using CFD". Proceedings of the AHS 50th Annual Forum and Technology Display, Washington, D.C., Vol. II:1259-1273, May 11-13, 1994.
- [17] Ramachandran, K., Schlechtriem, S., Caradonna, F. X. and Steinhoff, J. S. "The Application of Vorticity Embedding to the Computation of Advancing Rotor Flows". Paper presented at the American Helicopter Society 49th Annual Forum, St. Louis, MO, May 19-21, 1993.
- [18] Sani, R. L. and Gresho, P. M. Résumé and remarks on the open boundary condition minisymposium. *International Journal for Numerical Methods in Fluids*, 18:983-1008, 1994.
- [19] Steinhoff, J. S. and Suryanarayana, K. "The Treatment of Vortex Sheets in Compressible Potential Flow". Proceedings of the AIAA Symposium on Computational Fluid Dynamics, Danvers, July 1983.
- [20] Swarztrauber, P., Sweet, R. Efficient fortran programs for the solution of elliptic partial differential equations. Technical report, NCAR Technical Note-TN/IA-109, July 1975. see also <http://www.scd.ucar.edu/css/software/fishpack/technote.ps>.
- [21] Yanenko, N. N. *The Method of Fractional Steps*. Springer, New York - Berlin, 1971.

APPENDICES

Appendix A

Nomenclature

A.1 Symbols

AR : blade aspect ratio, $\frac{R}{c}$

\bar{a} : spreading distance

α : angle of attack

c_l : sectional lift coefficient

M_T : hover tip Mach number

p : pressure

\vec{q} : velocity vector

R : rotor tip radius

r : radial location

S_n : signed distance from grid point to
wake marker

u, v, w : velocity components in the x -, y -
and z - directions, respectively

Appendix A

Nomenclature

A.1 Symbols

AR : blade aspect ratio, $\frac{R}{c}$

\bar{a} : spreading distance

α : angle of attack

c_l : sectional lift coefficient

M_T : hover tip Mach number

p : pressure

\vec{q} : velocity vector

R : rotor tip radius

r : radial location

S_n : signed distance from grid point to
wake marker

u, v, w : velocity components in the x -, y -
and z - directions, respectively

- w_i : z-component of inflow velocity
- x, y, z : Cartesian coordinates
- Γ : bound circulation
- λ : shape function used in VE
- \mathbf{q} : fluid velocity vector, $(u, v, w)^T$
- Δ : uniform Cartesian grid spacing
- $\Delta\theta$: rotational increment
- σ : spreading function
- $\theta_{.75}$: collective pitch
- ϕ : velocity potential
- χ : location of wake node
- Ω : angular velocity of rotating blade
- ω : vorticity vector, $\nabla \times \mathbf{q}$
- ψ : wake age

A.2 Superscripts

- * or / : intermediate quantity
- ∞ : free-stream quantity
- ℓ : Lagrangian node
- n : time step
- T : rotor tip quantity
- v : vortical component

Appendix B

Image Point Convection

B.1 Equivalence with first upwind difference for appropriate Δt

The image point method of discretizing the convection equation in the first step of the fractional step method is equivalent to the explicit first order upwind scheme for appropriate Δt . In one dimension on a uniformly spaced grid, the method proceeds as follows:

$$u_i^{n+1} = I(u^n, \chi_i^{image})$$

where the interpolation function I is a function of the velocity field at time step n and the “image” point $\chi_i^{image} = x_i - \Delta t u_i^n$ at which u_i^{n+1} will be calculated. If $u_i > 0$ and Δt is appropriately small such that $|\Delta t u_i^n| < \Delta x$ then I is a function of u_{i-1}^n , u_i^n and the image point.

$$I = \frac{\Delta x - r_x}{\Delta x} u_{i-1}^n + \frac{r_x}{\Delta x} u_i^n$$

where $r_x = \chi_i^{image} - x_{i-1} = x_i - \Delta t u_i^n - x_{i-1} = \Delta x - \Delta t u_i^n$ is the distance between the image point and the grid point to the left of the image point. Therefore,

$$u_i^{n+1} = I = \frac{\Delta t u_i^n}{\Delta x} u_{i-1}^n + \frac{\Delta x - \Delta t u_i^n}{\Delta x} u_i^n$$

and after some rearranging,

$$u_i^{n+1} = u_i^n - \frac{\Delta t}{\Delta x} (u_i^n - u_{i-1}^n)$$

which is the first order explicit upwind scheme.

B.2 Stability

The image point method is a rare method in that it is both explicit and unconditionally stable. Its stability is derived from the fact that the image point at which the velocity is interpolated always lies in the appropriate domain of influence [5]. Therefore, it can be used for problems where the local CFL exceeds 1.0 whereas the first order upwind scheme becomes unstable. However, if the local CFL number exceeds 1.0 near a boundary, the appropriate domain of influence (and, hence, the image point) may lie outside the computational domain resulting in very interesting bus errors or segmentation faults. This might be alleviated with “ghost cells” outside of the computational region, but that point lies outside of the theoretical domain of this work.

¹Note that if $u_i < 0$ or $|\Delta t u_i^n| > \Delta x$ then “the grid point to the left of the image point” will not be x_{i-1} and the above formula for r_x will not hold.

Appendix C

“FISHPACK: A package of FORTRAN subprograms for the solution of separable elliptic partial differential equations”

The Poisson equations (2.6, 2.34) present in both the VE and FS grids are solved using the HW3CRT routine from the FISHPACK family of separable elliptic PDE solvers [20]. HW3CRT solves the standard seven-point finite difference approximation to the Helmholtz equation¹ on a three-dimensional non-staggered Cartesian grid. It is a fast direct solver for the discrete equation. The solver first Fourier transforms in the third dimension then utilizes cyclic reduction to solve a reduced set of equations. A non-staggered grid is used, because the scalar quantities resulting from both Poisson

¹The Poisson equation is a special case of the Helmholtz equation: $\nabla^2 \phi + \lambda \phi = F(x, y, z)$ where $\lambda = 0$.

equations are then differenced with a box scheme which takes the pressure at the grid nodes and returns the gradient of the pressure at the cell centers where the velocity vectors are located.

Appendix D

q^v Computation Module

In the q^v routine, it is necessary to prevent large fluctuations near the edges of the wake sheet. In order to minimize these fluctuations, it is necessary to determine whether particular grid points lie above, below, or outside the influence of the wake. It is necessary to have this information for the calculation of the gradient of the shape function, λ , as all of the points involved in this calculation have not necessarily been assigned a value and will need to be assigned a value of -.5 or .5. This is accomplished by examining the values of the array $facts(i,j,k)$ for each of the surrounding points. This array contains values of -1, 1, or 0 depending on whether the grid point in question is located "above", "below", or outside the influence of the wake. To this end, the following lines of code were executed at each (Eulerian) grid point for each wake sheet:

```
do 141 ii = 1,2
  id = ii + i - 1
  do 140 jj = 1,2
```

```

jd = jj +j-1
ivv(ii,jj,1) = facts(id,jd,k)
ivv(ii,jj,2) = facts(id,jd,k+1)
do 142 kk = 1,2
  do 139 l = 1,3
    if(ivv(ii,jj,kk).eq.1-2)nl(1)=nl(1)+1
  139 continue
  142 continue
140 continue
141 continue

```

For each grid point, nl(1) is the number of node points of the eight node points surrounding each cell center which are located "above" the wake. nl(2) is the number of node points outside the influence of the wake and nl(3) is the number "below" the wake. After the introduction of segmentation, this piece of code was executed at each grid point for each segment and required a ridiculously large number of operations. This code was replaced by the following pieces of code:

```

nl(2)=8-( facts(i,j,k)*facts(i,j,k)+
& facts(i+1,j,k)*facts(i+1,j,k)+
& facts(i+1,j+1,k)*facts(i+1,j+1,k)+
& facts(i+1,j+1,k+1)*facts(i+1,j+1,k+1)+
& facts(i+1,j,k+1)*facts(i+1,j,k+1)+
& facts(i,j,k+1)*facts(i,j,k+1)+
& facts(i,j+1,k+1)*facts(i,j+1,k+1)+
& facts(i,j+1,k)*facts(i,j+1,k) )

```

and

```

nl(3)=( (1+facts(i,j,k))*facts(i,j,k)+
&      (1+facts(i+1,j,k))*facts(i+1,j,k)+
&      (1+facts(i+1,j+1,k))*facts(i+1,j+1,k)+
&      (1+facts(i+1,j+1,k+1))*facts(i+1,j+1,k+1)+
&      (1+facts(i+1,j,k+1))*facts(i+1,j,k+1)+
&      (1+facts(i,j,k+1))*facts(i,j,k+1)+
&      (1+facts(i,j+1,k+1))*facts(i,j+1,k+1)+
&      (1+facts(i,j+1,k))*facts(i,j+1,k) ) / 2

```

nl(1) is just 8-nl(3) and is no longer calculated. Additionally, nl(3) is only calculated if the point in question is not either completely outside the influence of the wake or completely inside the influence of the wake (nl(2) is not equal to 0 or 8).

Vita

Jamie Ryan Kucab was born eight days late on April 9th, 1975.